

Chance-Constrained Sampling-Based MPC for Collision Avoidance in Uncertain Dynamic Environments

Ihab S. Mohamed, Mahmoud Ali, and Lantao Liu

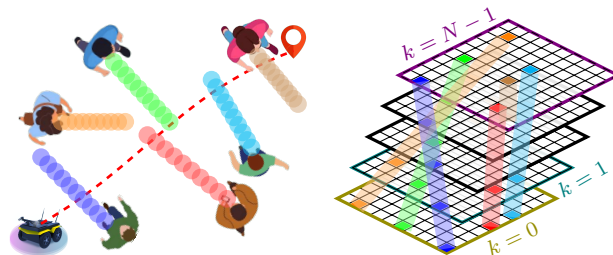
Abstract—Navigating safely in dynamic and uncertain environments is challenging due to uncertainties in perception and motion. This letter presents C^2U -MPPI, a robust sampling-based Model Predictive Control (MPC) framework that addresses these challenges by leveraging the Unscented Model Predictive Path Integral (U-MPPI) control strategy with integrated probabilistic chance constraints, ensuring more reliable and efficient navigation under uncertainty. Unlike gradient-based MPC methods, our approach (i) avoids linearization of system dynamics and directly applies non-convex and nonlinear chance constraints, enabling more accurate and flexible optimization, and (ii) enhances computational efficiency by reformulating probabilistic constraints into a deterministic form and employing a layered dynamic obstacle representation, enabling real-time handling of multiple obstacles. Extensive experiments in simulated and real-world human-shared environments validate the effectiveness of our algorithm against baseline methods, showcasing its capability to generate feasible trajectories and control inputs that adhere to system dynamics and constraints in dynamic settings, enabled by unscented-based sampling strategy and risk-sensitive trajectory evaluation. A supplementary video is available at: <https://youtu.be/FptAhvJlQm8>

Index Terms—Dense crowds, robot navigation, collision avoidance, optimization and optimal control

I. INTRODUCTION AND RELATED WORK

Nowadays, autonomous ground vehicles (AGVs) are increasingly deployed in complex, human-shared environments such as smart warehouses, autonomous driving, and urban logistics hubs. In these settings, AGVs must navigate toward designated goals while avoiding both static and dynamic obstacles. This task is particularly challenging due to uncertainties in predicting the future states of moving obstacles and potential localization errors, which complicate safety assessments of planned trajectories. As a result, AGVs must effectively balance safety and efficiency, underscoring the importance of *risk-aware* motion planning and control in unstructured, uncertain, and dynamic environments [1].

Numerous collision avoidance techniques have been developed to quantify and mitigate risks in dynamic environments, broadly classified into three main categories: reactive-based, optimization-based, and learning-based approaches [2]–[7]. Reactive-based methods, which rely on specific rules for collision avoidance, such as social forces [2] and artificial potential fields [3], are computationally efficient but often fail to capture human behavior accurately, sometimes resulting in unsafe or unnatural movements. In contrast, learning-based approaches aim to emulate and anticipate human behavior but encounter challenges in unfamiliar scenarios due to their dependence on prior training data [4]. Furthermore, both approaches typically neglect the robot’s kinodynamic constraints, limiting their effectiveness in complex or high-speed scenarios. Optimization-based methods, particularly Model



(a) LKF-based pedestrian predictions (b) Layered obstacle representation
Fig. 1: Handling dynamic obstacles by (a) predicting pedestrian positions using LKF and (b) structuring them into a layered representation for efficient trajectory evaluation over the prediction horizon N .

Predictive Control (MPC), have emerged as prominent solutions to address these limitations, effectively integrating the robot kinodynamic constraints with both static and dynamic collision constraints. This integration enables simultaneous planning and control, generating an optimal trajectory that balances safety and efficiency [5]–[7]. Such methods involve two sequential steps at each time-step: first, utilizing a motion model to predict dynamic obstacles in the environment, and second, formulating the robot’s navigation task as an optimal control problem [6]. Nevertheless, a critical challenge with these methods lies in guaranteeing safety within the generated trajectories, particularly given their limited capacity to account for uncertainties in perception and motion.

Control Barrier Functions (CBFs) [8], [9] and Chance Constraints (CCs) [10], [11] are widely recognized as effective methodologies for enhancing safety within MPC-based frameworks by integrating safety-critical constraints into the optimization process. CBFs dynamically adjust control inputs to maintain system states within predefined safe sets, considering worst-case scenarios of uncertainty to ensure safety and constraint satisfaction; however, they often lead to overly conservative control actions in highly uncertain, dynamic environments, potentially resulting in low system performance or infeasible solutions [12]. Recent works, including the softening of hard constraints through exact penalties [9], slack variable relaxations [13], and generalized CBFs [14], have effectively mitigated CBF infeasibility issues while enhancing safety in crowded and dynamic scenarios. On the other hand, CCs address the limitations of CBFs by providing probabilistic safety guarantees, allowing limited violations as long as the probability of such violations remains below an acceptable threshold [15]. Despite their advantages, CCs face challenges such as computational complexity and conservatism associated with probabilistic modeling and fixed thresholds for constraint violations, which constrain their scalability in dynamic and high-dimensional environments [10]. To address these limitations, [16] introduced a computationally efficient real-time framework for chance-constrained optimization by leveraging a simplified probabilistic model to manage dynamic obstacles, while [11], [15] achieved similar improvements by dynami-

Authors are with the Luddy School of Informatics, Computing, and Engineering, Indiana University, Bloomington, IN 47408 USA (e-mail: {mohamedi, alimaa, lantao}@iu.edu)

cally adjusting risk thresholds to balance safety and efficiency in real-time. Additionally, [17] developed a distributionally robust chance-constrained MPC framework that incorporates Conditional Value at Risk (CVaR) to address predictive motion uncertainties and mitigate the conservatism of Gaussian distribution assumptions. Yet, as the number of dynamic obstacles increases, the dimensionality of constraints grows rapidly, significantly reducing the performance of MPC and increasing the likelihood of infeasible solutions [5], [10]. Furthermore, both system dynamics and probabilistic constraints often require linearization to convert the optimization problem into a convex form, ensuring computational traceability [11].

To mitigate the challenges posed by gradient-based MPC methods, this letter introduces a new avenue for sampling-based MPC approaches that make no assumptions or approximations on objective functions and system dynamics [18], targeting autonomous navigation in crowded environments. Specifically, we propose C²U-MPPI, an extension of our U-MPPI algorithm [12] which incorporates probabilistic chance constraints into the optimization framework to enhance collision avoidance under uncertainty while preserving computational efficiency. By leveraging the Unscented Transform (UT) for trajectory sampling and integrating risk-sensitive trajectory evaluation, our method generates more feasible trajectories that account for both static and dynamic obstacles, enabling robust and adaptive navigation in uncertain environments. The main contributions of this work are summarized as follows:

- 1) A real-time collision avoidance method for dynamic and uncertain environments is proposed by extending the U-MPPI framework with probabilistic collision checking, reformulated in Section III-B into a computationally efficient deterministic form for seamless integration.
- 2) Dynamic collision avoidance costs are introduced for MPPI-based algorithms in Section III-C, evaluating sampled trajectories based on their interactions with dynamic obstacles and thereby enhancing navigation robustness.
- 3) A layered dynamic obstacle representation is proposed to efficiently evaluate trajectories over a prediction horizon, enabling real-time handling of multiple obstacles, as detailed in Section III-D and illustrated in Fig. 1.
- 4) The proposed control strategy is validated through simulations and real-world experiments in Section IV, demonstrating its effectiveness in both cooperative and non-cooperative scenarios compared to baseline methods.

II. PRELIMINARIES

This section introduces the robot motion and obstacle models along with the trajectory planning problem formulation.

A. Robot Motion Model

In this work, we address the problem of trajectory planning and collision avoidance for a single AGV navigating in a 2D unknown environment $\mathcal{W} \subset \mathbb{R}^2$ with both static and dynamic obstacles. The robot's dynamics are governed by a nonlinear discrete-time stochastic dynamical system, described as:

$$\mathbf{x}_{k+1} = f(\mathbf{x}_k, \mathbf{u}_k + \delta \mathbf{u}_k), \quad (1)$$

where $\mathbf{x}_k = [\mathbf{p}_k^\top, \theta_k]^\top \in \mathbb{R}^{n_x}$ represents the state of the robot at time-step k , encompassing its position $\mathbf{p}_k = [x_k, y_k]^\top$ and orientation θ_k , and $\mathbf{u}_k \in \mathbb{R}^{n_u}$ denotes the control input.

The control input is subject to disturbances, modeled as additive zero-mean Gaussian noise $\delta \mathbf{u}_k$ with covariance $\Sigma_{\mathbf{u}}$, capturing the uncertainty in the system's actuation. Considering a finite time-horizon N , the sequence of control inputs \mathbf{U} is represented as $\mathbf{U} = [\mathbf{u}_0, \mathbf{u}_1, \dots, \mathbf{u}_{N-1}]^\top \in \mathbb{R}^{n_u N}$, while the corresponding state trajectory of the system is $\mathbf{x} = [\mathbf{x}_0, \mathbf{x}_1, \dots, \mathbf{x}_N]^\top \in \mathbb{R}^{n_x(N+1)}$. The area occupied by the robot at state \mathbf{x}_k , denoted $\mathcal{X}^{\text{rob}}(\mathbf{x}_k) \subset \mathcal{W}$, is approximated as a circular region $\mathcal{A}(\mathbf{p}_k, r_r)$, centered at \mathbf{p}_k with radius r_r .

B. Dynamic and Static Obstacles Model

The environment $\mathcal{W} \subset \mathbb{R}^2$ is characterized by the presence of dynamic obstacles, specifically human pedestrians, which are modeled as non-cooperative agents with uncertain motion trajectories. Each dynamic obstacle at time-step k is represented by its state \mathbf{o}_k^i , where $i \in \{1, 2, \dots, N_o\}$ indexes the i -th obstacle. For each dynamic obstacle \mathbf{o}^i , the area it occupies, $\mathcal{O}_{k,i}^{\text{dyn}} \subset \mathcal{W}$, is modeled as a circle with center $\mathbf{p}_k^i = [x_k^i, y_k^i]^\top$ and radius r_o^i . The state evolution of each obstacle follows a state transition function $\xi(\cdot)$, defined as $\mathbf{o}_{k+1}^i = \xi(\mathbf{o}_k^i)$, which governs the dynamics of the system. As in [5], the motion of human pedestrians is assumed to follow a constant velocity model, expressed as $\dot{\mathbf{p}}^i = \omega^i$, where $\omega^i \sim \mathcal{N}(0, \Sigma_o^o)$ represents zero-mean Gaussian noise with diagonal covariance matrix $\Sigma_o^o \in \mathbb{R}^2$. This implies that the acceleration is solely driven by the noise term, reflecting the uncertainty in pedestrian motion. Using observed position data, the future positions and associated uncertainties of the obstacles are estimated and predicted through a standard Linear Kalman Filter (LKF) [19], enabling the modeling of human motion in dynamic environments with inherent uncertainties. To reflect a realistic scenario, we assume that the robot navigates in an unknown or partially observed environment. Consequently, a robot-centered 2D occupancy grid map (i.e., local costmap) is constructed and continuously updated based on incoming sensory data to record static obstacles in the robot's surroundings, with the area occupied by static obstacles denoted as $\mathcal{O}^{\text{stc}} \subset \mathcal{W}$. To avoid overlap between static and dynamic collision constraints and reduce noise from increasing pedestrian numbers in the costmap, (i) detected pedestrians are filtered from the point cloud and classified as dynamic agents, and (ii) the local costmap is then generated for static obstacles.

C. Problem Formulation

Given the cost function J , the occupied spaces of the robot $\mathcal{X}^{\text{rob}}(\mathbf{x}_k)$, the dynamic obstacles $\mathcal{O}_k^{\text{dyn}} = \bigcup_{i=1}^{N_o} \mathcal{O}_{k,i}^{\text{dyn}}$, and the static obstacles \mathcal{O}^{stc} , along with the initial and desired states \mathbf{x}_s and \mathbf{x}_f , the objective is to compute the optimal control sequence $\mathbf{U} = \{\mathbf{u}_k\}_{k=0}^{N-1}$ that enables the robot to safely and efficiently navigate from \mathbf{x}_s to \mathbf{x}_f , while avoiding collisions with both static and dynamic obstacles. The resulting optimization problem is formalized as follows:

$$\min_{\mathbf{U}} J = \mathbb{E} \left[\phi(\mathbf{x}_N) + \sum_{k=0}^{N-1} \left(q(\mathbf{x}_k) + \frac{1}{2} \mathbf{u}_k^\top R \mathbf{u}_k \right) \right], \quad (2a)$$

$$\text{s.t. } \mathbf{x}_{k+1} = f(\mathbf{x}_k, \mathbf{u}_k + \delta \mathbf{u}_k), \delta \mathbf{u}_k \sim \mathcal{N}(\mathbf{0}, \Sigma_{\mathbf{u}}), \quad (2b)$$

$$\mathbf{x}_0 = \mathbf{x}_s, \quad \mathbf{u}_k \in \mathbb{U}, \quad \mathbf{x}_k \in \mathbb{X}, \quad (2c)$$

$$\mathcal{X}^{\text{rob}}(\mathbf{x}_k) \cap (\mathcal{O}^{\text{stc}} \cup \mathcal{O}_k^{\text{dyn}}) = \emptyset, \quad (2d)$$

where J denotes the expected value of the cost function,

comprising the terminal state cost $\phi(\mathbf{x}_N)$, an arbitrary state-dependent cost $q(\mathbf{x}_k)$, and the quadratic control cost $\frac{1}{2}\mathbf{u}_k^\top R\mathbf{u}_k$, where $R \in \mathbb{R}^{n_u \times n_u}$ is a positive-definite weighting matrix. The optimization accounts for the system dynamics specified in (2b), while ensuring that the control inputs \mathbf{u}_k and states \mathbf{x}_k remain within their respective feasible sets or constraint sets \mathbb{U} and \mathbb{X} , as described in (2c), and ensures collision avoidance, as outlined in (2d). Recall that the robot and obstacles are modeled as circles, with the robot centered at $\mathbf{p}_k = [x_k, y_k]^\top$ and each obstacle \mathbf{o}_k^i centered at $\mathbf{p}_k^i = [x_k^i, y_k^i]^\top$, and having radii r_r and r_o^i , respectively. Consequently, the minimum safe distance between the robot and the moving obstacle \mathbf{o}^i is given by $r_{\text{safe}}^i = r_r + r_o^i$. Thus, the collision avoidance constraint for dynamic obstacles, expressed as $\mathcal{X}^{\text{rob}}(\mathbf{x}_k) \cap \mathcal{O}_k^{\text{dyn}} = \emptyset$ in (2d), can be formulated as:

$$g_i(\mathbf{x}_k, \mathbf{o}_k^i) = \|\mathbf{x}_k - \mathbf{o}_k^i\|_2 - r_{\text{safe}}^i, \quad (3)$$

where ensuring that $g_i(\mathbf{x}_k, \mathbf{o}_k^i) \geq 0$ at each time-step k guarantees that the robot maintains a safe distance from obstacle \mathbf{o}^i , thus preventing collisions.

D. MPPI Algorithm Overview

MPPI seeks to minimize the cost function J defined in (2) by sampling control inputs and forward-propagating M trajectories through the system dynamics over a prediction horizon of N . The optimal control sequence $\{\mathbf{u}_k\}_{k=0}^{N-1}$ is iteratively updated using a weighted sum of control perturbations:

$$\mathbf{u}_k \leftarrow \mathbf{u}_k + \sum_{m=1}^M w_m \delta \mathbf{u}_{k,m}, \quad (4)$$

where w_m represents the weight assigned to each trajectory, computed based on the trajectory cost S_m as:

$$w_m = \frac{\exp\left(-\frac{1}{\lambda}(S_m - S_{\min})\right)}{\sum_{k=1}^M \exp\left(-\frac{1}{\lambda}(S_m - S_{\min})\right)}, \quad (5)$$

with λ controlling sensitivity to cost differences and S_{\min} represents the minimum cost among all the sampled trajectories. The *cost-to-go* of the m -th trajectory is calculated as:

$$S_m = \phi(\mathbf{x}_N) + \sum_{k=0}^{N-1} \tilde{q}(\mathbf{x}_k, \mathbf{u}_k, \delta \mathbf{u}_{k,m}) \quad \forall m \in \{1, \dots, M\}, \quad (6)$$

where $\tilde{q}(\mathbf{x}_k, \mathbf{u}_k, \delta \mathbf{u}_{k,m})$ includes both the state-dependent running cost $q(\mathbf{x}_k)$ and the quadratic control cost $q_u(\mathbf{u}_k, \delta \mathbf{u}_k)$ associated with the control perturbation $\delta \mathbf{u}_{k,m}$.

III. PROPOSED C²U-MPPI FRAMEWORK

In this section, we present our proposed chance-constrained U-MPPI control strategy, incorporating dynamic costs and a layered obstacle representation for navigation under uncertainty.

A. U-MPPI Control Algorithm

The U-MPPI algorithm [12] enhances classical MPPI by optimizing control inputs under uncertainty through the integration of the UT, which propagates both the mean $\hat{\mathbf{x}}_k$ and covariance Σ_k^x of the system dynamics, with $\mathbf{x}_k \sim \mathcal{N}(\hat{\mathbf{x}}_k, \Sigma_k^x)$, enabling more efficient trajectory sampling and improved state-space exploration. Additionally, U-MPPI incorporates a risk-sensitive cost function that adjusts control actions based on a risk-sensitivity parameter γ , where $\gamma > 0$ leads to risk-seeking behavior and $\gamma < 0$ induces risk-averse behavior.

Building on this foundation, the U-MPPI control loop oper-

ates by estimating the current system state $\mathbf{x}_0 \sim \mathcal{N}(\hat{\mathbf{x}}_0, \Sigma_0^x)$ and generating $N \times M_\sigma$ random control perturbations $\delta \mathbf{u}$. It then samples M_σ batches in parallel on the GPU, with each batch containing n_σ trajectories, resulting in a total of $M = n_\sigma M_\sigma$ rollouts, where $n_\sigma = 2n_x + 1$ represents the number of sigma points. For each batch $m \in \{1, \dots, M_\sigma\}$, the state distribution $\mathbf{x}_k \sim \mathcal{N}(\hat{\mathbf{x}}_k, \Sigma_k^x)$ is approximated using n_σ sigma points $\{\mathcal{X}_k^{(i)}\}_{i=0}^{2n_x}$ at each time-step k . These sigma points are computed as $\mathcal{X}_k^{(0)} = \hat{\mathbf{x}}_k$, $\mathcal{X}_k^{(i)} = \hat{\mathbf{x}}_k + (\sqrt{(n_x + \lambda_\sigma)\Sigma_k^x})_i$ for $i = 1, \dots, n_x$, and $\mathcal{X}_k^{(i)} = \hat{\mathbf{x}}_k - (\sqrt{(n_x + \lambda_\sigma)\Sigma_k^x})_i$ for $i = n_x + 1, \dots, 2n_x$, where $\lambda_\sigma = \alpha^2(n_x + k_\sigma) - n_x$, with λ_σ influenced by the scaling parameters $k_\sigma \geq 0$ and $\alpha \in (0, 1]$, which control the dispersion of the sigma points around the mean. The sigma points are propagated through the underlying nonlinear dynamics described in (1), as $\mathcal{X}_{k+1}^{(i)} = f(\mathcal{X}_k^{(i)}, \mathbf{u}_k + \delta \mathbf{u}_k)$, which can be compactly written as $\mathbf{X}_{k+1} = \mathbf{f}(\mathbf{X}_k, \mathbf{u}_k + \delta \mathbf{u}_k)$, where $\mathbf{X}_{k+1} = [\mathcal{X}_{k+1}^{(0)}, \dots, \mathcal{X}_{k+1}^{(2n_x)}]^\top \in \mathbb{R}^{n_x n_\sigma}$. After propagation, the sigma points are converted back into the mean and covariance using $\hat{\mathbf{x}}_{k+1} = \sum_{i=0}^{2n_x} w_m^{(i)} \mathcal{X}_{k+1}^{(i)}$ and $\Sigma_{k+1}^x = \sum_{i=0}^{2n_x} w_c^{(i)} (\mathcal{X}_{k+1}^{(i)} - \hat{\mathbf{x}}_{k+1})(\mathcal{X}_{k+1}^{(i)} - \hat{\mathbf{x}}_{k+1})^\top$, where $w_m^{(i)}$ and $w_c^{(i)}$ are weights for computing the mean and covariance, respectively; these weights are defined as $w_m^{(0)} = \frac{\lambda_\sigma}{n_x + \lambda_\sigma}$, $w_c^{(0)} = w_m^{(0)} + (1 - \alpha^2 + \beta)$, and $w_m^{(i)} = w_c^{(i)} = \frac{1}{2(n_x + \lambda_\sigma)}$ for $i = 1, \dots, 2n_x$, where β is a hyper-parameter that balances the importance of mean and covariance. This sequential process, repeated throughout the entire time-horizon N , ensures the accurate propagation of both the mean and covariance of the state distribution, yielding a sequence of state vectors $\{\mathbf{X}_1, \mathbf{X}_2, \dots, \mathbf{X}_N\} \equiv \{\mathbf{X}_k\}_{k=1}^N$, which represents a batch of n_σ sampled trajectories.

By propagating the system uncertainty Σ_k^x , U-MPPI integrates this uncertainty into trajectory evaluation using a risk-sensitive state-dependent cost function to assess the i -th trajectory in each batch:

$$q_{\text{rs}}(\mathcal{X}_k^{(i)}, \Sigma_k^x) = \frac{1}{\gamma} \log \det(\mathbf{I} + \gamma Q \Sigma_k^x) + \left\| \mathcal{X}_k^{(i)} - \mathbf{x}_f \right\|_{Q_{\text{rs}}}^2, \quad (7)$$

where $Q_{\text{rs}}(\Sigma_k^x) = (Q^{-1} + \gamma \Sigma_k^x)^{-1}$ is the risk-sensitive penalty coefficient matrix, determined by the risk-sensitivity parameter γ that modulates U-MPPI's sensitivity to uncertainty. It adjusts how the algorithm balances the trade-off between risk and reward when evaluating trajectories. For instance, when $\gamma < 0$, the penalty matrix Q_{rs} increases with higher system uncertainty Σ_k^x , resulting in a larger q_{rs} and imposing greater penalties for deviations from the desired state \mathbf{x}_f . The *cost-to-go* of trajectory $\tau_m^{(i)}$ in batch m is defined as:

$$S(\tau_m^{(i)}) = \phi(\mathcal{X}_N^{(i)}) + \sum_{k=0}^{N-1} \tilde{q}(\mathcal{X}_k^{(i)}, \Sigma_k^x, \mathbf{u}_k, \delta \mathbf{u}_{k,m}), \quad (8)$$

$$\forall m \in \{1, \dots, M_\sigma\}, \quad \forall i \in \{0, \dots, 2n_x\},$$

where the state-dependent cost $q(\mathcal{X}_k^{(i)}, \Sigma_k^x)$ incorporated in \tilde{q} now derives from the risk-sensitive cost q_{rs} , while retaining the original quadratic control term $q_u(\mathbf{u}_k, \delta \mathbf{u}_k)$. In this work, the control cost is defined as $q_u(\mathbf{u}_k, \delta \mathbf{u}_k) = \gamma_u \delta \mathbf{u}_{k,i}^\top R \delta \mathbf{u}_{k,i} + \mathbf{u}_k^\top R \delta \mathbf{u}_{k,i} + \frac{1}{2} \mathbf{u}_k^\top R \mathbf{u}_k$, where $\gamma_u = \frac{\nu-1}{2\nu} \in \mathbb{R}_{\geq 0}$, and $\nu \geq 1$ controls the level of aggressiveness in exploring the state-space [20]. The control input sequence in U-MPPI is updated

using the same weighted averaging method as in MPPI:

$$\mathbf{u}_k \leftarrow \mathbf{u}_k + \frac{\sum_{m=1}^{M_\sigma} \exp\left(\frac{-1}{\lambda}(\mathbf{S}(\tau_m) - S_{\min})\right) \delta \mathbf{u}_{k,m}}{\sum_{m=1}^{M_\sigma} \exp\left(\frac{-1}{\lambda}(\mathbf{S}(\tau_m) - S_{\min})\right)}, \quad (9)$$

where $\mathbf{S}(\tau_m) = [S(\tau_m^{(0)}), \dots, S(\tau_m^{(2n_x)})]^\top \in \mathbb{R}^{n_\sigma}$ represents the costs of all sigma-point trajectories within batch m . The optimal control sequence $\{\mathbf{u}_k\}_{k=0}^{N-1}$ is smoothed with a Savitzky-Golay filter, then the first control \mathbf{u}_0 is applied to the system, and the remaining $N-1$ steps are shifted as a warm-start for the next control loop. Building on these concepts, the stochastic optimal control problem in (2) is reformulated within the unscented guidance framework as follows:

$$\min_{\mathbf{U}} \mathbf{J}(\mathbf{X}, \mathbf{u}) = \mathbb{E} \left[\Phi(\mathbf{X}_N) + \sum_{k=0}^{N-1} \left(\mathbf{q}(\mathbf{X}_k) + \frac{1}{2} \mathbf{u}_k^\top \mathbf{R} \mathbf{u}_k \right) \right], \quad (10a)$$

$$\text{s.t. } \mathbf{X}_{k+1} = \mathbf{f}(\mathbf{X}_k, \mathbf{u}_k + \delta \mathbf{u}_k), \delta \mathbf{u}_k \sim \mathcal{N}(\mathbf{0}, \Sigma_{\mathbf{u}}), \quad (10b)$$

$$\Pr(C) \leq \delta \quad \text{and} \quad \mathcal{X}^{\text{rob}}(\mathbf{X}_k) \cap \mathcal{O}^{\text{stc}} = \emptyset, \quad (10c)$$

$$\mathbf{X}_0 = [\mathcal{X}_0^{(0)}, \dots, \mathcal{X}_0^{(2n_x)}]^\top, \mathbf{u}_k \in \mathbb{U}, \mathbf{X}_k \in \mathbb{X}, \quad (10d)$$

where $\Phi(\mathbf{X}_N) = [\phi(\mathcal{X}_N^{(0)}), \dots, \phi(\mathcal{X}_N^{(2n_x)})]^\top \in \mathbb{R}^{n_\sigma}$ and $\mathbf{q}(\mathbf{X}_k) = [q(\mathcal{X}_k^{(0)}), \dots, q(\mathcal{X}_k^{(2n_x)})]^\top \in \mathbb{R}^{n_\sigma}$. For further details on U-MPPI and the impact of parameters γ , α , and k_σ on its performance, refer to [12].

B. Robot-Obstacle Collision Avoidance Chance Constraints

For MPPI, the collision avoidance condition in (3) assumes deterministic obstacle and robot positions based on known or predicted locations, ensuring collision-free sampled trajectories but neglects uncertainties in position estimates. In contrast, U-MPPI incorporates uncertainty through the UT, allowing for a probabilistic assessment of collision risks, making it more suitable for uncertain environments. To further improve it, we replace the deterministic collision constraint with probabilistic collision checking, formulated as a chance constraint $\Pr(C) \leq \delta$ in (10c), where $C(\mathbf{p}_k, \mathbf{p}_k^i) : \|\mathbf{p}_k - \mathbf{p}_k^i\| \leq r_{\text{safe}}^i$ defines the collision condition between robot position \mathbf{p}_k and i -th obstacle position \mathbf{p}_k^i , and $\delta \in \mathbb{R}^+$ sets the confidence level for avoidance. To simplify the analysis, we retain the robot as a disk with its area defined by $\mathcal{A}(\mathbf{p}_k, r_r)$, while modeling the obstacle as a point located at $\mathbf{p}_k^i = [x_k^i, y_k^i]^\top$. Accordingly, the collision condition is given by $C : \mathbf{p}_k^i \in \mathcal{A}(\mathbf{p}_k, r_r)$. The instantaneous collision probability is derived from the joint distribution of the robot and obstacle positions:

$$\Pr(C) = \int_{\mathbf{p}_k} \int_{\mathbf{p}_k^i} \mathbb{I}_c(\mathbf{p}_k^i, \mathbf{p}_k) p(\mathbf{p}_k, \mathbf{p}_k^i) d\mathbf{p}_k d\mathbf{p}_k^i, \quad (11)$$

where $p(\mathbf{p}_k, \mathbf{p}_k^i) = p(\mathbf{p}_k^i | \mathbf{p}_k) p(\mathbf{p}_k)$ represents the joint likelihood of the robot being at \mathbf{p}_k and the obstacle at \mathbf{p}_k^i and \mathbb{I}_c is the indicator function defined as:

$$\mathbb{I}_c(\mathbf{p}_k^i, \mathbf{p}_k) = \begin{cases} 1, & \text{if } \mathbf{p}_k^i \in \mathcal{A}(\mathbf{p}_k, r_r), \\ 0, & \text{otherwise.} \end{cases} \quad (12)$$

By applying the indicator function \mathbb{I}_c and expanding the joint distribution, the probability of collision can be formulated as:

$$\Pr(C) = \int_{\mathbf{p}_k} \left[\int_{\mathbf{p}_k^i \in \mathcal{A}(\mathbf{p}_k, r_r)} p(\mathbf{p}_k^i | \mathbf{p}_k) d\mathbf{p}_k^i \right] p(\mathbf{p}_k) d\mathbf{p}_k. \quad (13)$$

To efficiently solve the integral in (13), we apply two simplifying assumptions that reflect the system's inherent

characteristics, such as the robot's compact size, and align with the U-MPPI framework, which models system states as Gaussian distributions. First, by assuming the robot has a small radius, we approximate the inner integral as:

$$\int_{\mathbf{p}_k^i \in \mathcal{A}(\mathbf{p}_k, r_r)} p(\mathbf{p}_k^i | \mathbf{p}_k) d\mathbf{p}_k^i \approx A_r p(\mathbf{p}_k^i = \mathbf{p}_k | \mathbf{p}_k), \quad (14)$$

where $A_r = \pi r_r^2$ represents the area of the region $\mathcal{A}(\mathbf{p}_k, \varepsilon)$, and $p(\mathbf{p}_k^i = \mathbf{p}_k | \mathbf{p}_k)$ denotes the conditional distribution of the obstacle evaluated at the robot's position \mathbf{p}_k . Given this approximation, the probability of collision becomes:

$$\Pr(C) \approx A_r \int_{\mathbf{p}_k} p(\mathbf{p}_k^i = \mathbf{p}_k | \mathbf{p}_k) p(\mathbf{p}_k) d\mathbf{p}_k. \quad (15)$$

Next, assuming that the uncertainties in the positions of the robot and the obstacle are independently modeled by Gaussian distributions (i.e., $\mathbf{p}_k \sim \mathcal{N}(\hat{\mathbf{p}}_k, \Sigma_k^x)$ and $\mathbf{p}_k^i \sim \mathcal{N}(\hat{\mathbf{p}}_k^i, \Sigma_k^o)$), the probability of collision can be further approximated as:

$$\Pr(C) \approx \frac{A_r}{\eta_c} \exp\left(-\frac{1}{2}(\hat{\mathbf{p}}_k - \hat{\mathbf{p}}_k^i)^\top \Sigma_k^{c-1} (\hat{\mathbf{p}}_k - \hat{\mathbf{p}}_k^i)\right), \quad (16)$$

where $\Sigma_k^c \triangleq \Sigma_k^x + \Sigma_k^o$ denotes the combined covariance of the two distributions, and $\eta_c \triangleq \sqrt{\det(2\pi \Sigma_k^c)}$ [10]. Building on the derived approximation in (16), the chance constraint for collision avoidance, $\Pr(C) \leq \delta$, can be expressed as:

$$\|\hat{\mathbf{p}}_k - \hat{\mathbf{p}}_k^i\|_{\Sigma_k^{c-1}}^2 \geq \kappa(\Sigma_k^c, A_r, \delta), \quad (17)$$

where $\|\hat{\mathbf{p}}_k - \hat{\mathbf{p}}_k^i\|_{\Sigma_k^{c-1}}^2 = (\hat{\mathbf{p}}_k - \hat{\mathbf{p}}_k^i)^\top \Sigma_k^{c-1} (\hat{\mathbf{p}}_k - \hat{\mathbf{p}}_k^i)$ and $\kappa(\Sigma_k^c, A_r, \delta) = -2 \ln\left(\frac{\eta_c \delta}{A_r}\right)$ is a deterministic scalar threshold computed at each time-step k as a function of Σ_k^c , A_r , and δ . The inequality shown in (17) serves as a deterministic collision avoidance constraint, requiring the robot's mean position $\hat{\mathbf{p}}_k$ to remain outside the ellipsoidal safety boundary centered at the mean position of the obstacle $\hat{\mathbf{p}}_k^i$. As a result, the probabilistic constraint $\Pr(C) \leq \delta$ in (10c) is effectively reformulated into a computationally feasible deterministic form that integrates seamlessly into the U-MPPI framework, ensuring safe navigation under uncertainty.

Notably, unlike many approximation approaches that uniformly inflate the robot and obstacle geometries across all dimensions to serve as a "safety cushion", our method enables a more precise and dimension-specific construction and tracking of the safety buffer. This is accomplished by dynamically assessing and updating the uncertainty Σ_k^c in real time.

C. Cost Function Design

In sampling-based MPC approaches, the state-dependent running cost $q(\cdot)$ serves as a key component in directing the robot's behavior by penalizing undesired states. For safe, goal-driven navigation in a 2D environment with static and dynamic obstacles, we evaluate each sampled trajectory as:

$$q(\cdot) = q_{\text{goal}}(\cdot) + q_{\text{stc}}(\cdot) + q_{\text{dyn}}(\cdot), \quad (18)$$

which is composed of three terms: goal-directed cost $q_{\text{goal}}(\cdot)$, and collision avoidance costs for static and dynamic obstacles, $q_{\text{stc}}(\cdot)$ and $q_{\text{dyn}}(\cdot)$, respectively. Here, (\cdot) in $q(\cdot)$ specifically refers to (\mathbf{x}_k) in MPPI and $(\mathcal{X}_k^{(i)}, \Sigma_k^x)$ in U-MPPI. The first term $q_{\text{goal}}(\cdot)$ penalizes the robot's deviation from the desired goal state \mathbf{x}_f . In MPPI, q_{goal} is expressed as the standard quadratic cost, given by $q_{\text{goal}}(\mathbf{x}_k) = \|\mathbf{x}_k - \mathbf{x}_f\|_Q^2$, whereas U-MPPI employs the risk-sensitive cost $q_{\text{rs}}(\mathcal{X}_k^{(i)}, \Sigma_k^x)$, as

specified in (7). In both control strategies, the second term q_{stc} is defined as $q_{\text{stc}}(\mathbf{x}) = w_{\text{stc}} \mathbb{I}_{\text{stc}}$, acting as an indicator function that applies a high penalty weight w_{stc} when the robot collides with static obstacles, where $\mathbb{I}_{\text{stc}} = 1$ if $\mathcal{X}^{\text{rob}}(\mathbf{x}) \cap \mathcal{O}^{\text{stc}} \neq \emptyset$, with \mathbf{x} representing \mathbf{x}_k in MPPI and $\mathcal{X}_k^{(i)}$ in U-MPPI. In [21], we employed the first two terms of $q(\cdot)$ to achieve collision-free navigation in dynamic environments using a 2D local costmap from local perception. However, as the number of moving agents increased, the costmap became noisier, increasing the risk of local minima traps.

To address these limitations and enhance safety in dynamic environments, we propose a dynamic collision avoidance cost, q_{dyn} , which incorporates one or more of the following cost functions: exponential-shaped q_{exp} , repulsive q_{rep} , and probabilistic collision-checking q_{prob} , thereby offering a more robust and reliable navigation solution. The respective cost functions are mathematically defined as follows:

$$q_{\text{exp}}(\mathbf{x}_k) = w_{\text{exp}} \sum_{i=1}^{N_o} \exp\left(-\alpha_{\text{exp}}\left(\|\mathbf{p}_k - \mathbf{p}_k^i\| - r_{\text{safe}}^i\right)\right), \quad (19)$$

$$q_{\text{rep}}(\mathbf{x}_k) = w_{\text{rep}} \sum_{i=1}^{N_o} \left(\frac{1}{\|\mathbf{p}_k - \mathbf{p}_k^i\|^2 + \gamma_{\text{rep}}}\right), \quad (20)$$

$$q_{\text{prob}}(\mathcal{X}_k^{(i)}, \Sigma_k^{\mathbf{x}}) = w_{\text{prob}} \begin{cases} 1, & \text{if } \|\hat{\mathbf{p}}_k - \hat{\mathbf{p}}_k^i\|_{\Sigma_k^{\mathbf{c}}^{-1}}^2 < \kappa, \\ 0, & \text{otherwise,} \end{cases} \quad (21)$$

where w_{exp} , w_{rep} and w_{prob} are the collision penalty weighting coefficients determining the influence of each cost function, α_{exp} adjusts the sharpness of the exponential penalties, and γ_{rep} serves as a stabilizing constant to prevent singularities in q_{rep} . The first two trajectory assessment functions impose heavily weighted penalties on trajectories that violate the collision avoidance condition $g_i(\mathbf{x}_k, \mathbf{o}_k^i) \geq 0$ in (3), ensuring the robot maintains a safe distance from obstacles. The first, q_{exp} , enforces strict avoidance with a sharp exponential penalty near obstacles, while the second, q_{rep} , employs a potential function with an inverse-square penalty to repel the robot. Additionally, q_{rep} enhances clearance from moving obstacles, providing an extra layer of safety and balancing avoidance with smooth motion planning, enabling effective navigation without abrupt maneuvers [5]. In contrast, the third objective, q_{prob} , applies a stringent binary penalty using probabilistic collision-checking from (17), heavily penalizing trajectories that violate the risk threshold κ to ensure safety under uncertainty. While the proposed trajectory assessment functions are deterministic, it is important to note that the first two are applicable to both control strategies,¹ whereas the third is exclusive to U-MPPI due to its ability to propagate system uncertainty $\Sigma_k^{\mathbf{x}}$.

D. Dynamic Obstacle Representation

In gradient-based MPC algorithms such as MPCC [5], dynamic obstacles are addressed by explicitly incorporating their predicted positions as constraints in the trajectory planning optimization process, ensuring collision-free navigation by avoiding intersections with the predicted obstacle paths. However, as the number of obstacles increases, the corresponding rise in constraints significantly expands the problem's dimensionality, leading to higher computational demands and thus limiting the

number of obstacles the algorithm can effectively manage. In contrast, we propose a more scalable solution that leverages the parallel nature of sampling and GPU-based computation. Inspired by the environment representation in [18], our approach employs a layered structure for obstacle predictions over the control time-horizon N , with each layer representing the positions of obstacles at a specific time, as depicted in Fig. 1(b). Rather than directly constraining predicted positions from the LKF, as in Fig. 1(a), we evaluate sampled trajectories based on the corresponding obstacle layer at each time step. For instance, at $k = 3$, the control algorithm considers only the third layer of predictions to compute $q_{\text{dyn}}(\cdot)$. To address discrepancies between the prediction horizon of the pedestrians and the controller, linear interpolation is used to align them before transforming the predictions into layers. Such a solution enables the consideration of more obstacles in optimization while maintaining flexible trajectory evaluation and real-time performance in dynamic, uncertain environments.

IV. RESULTS AND ANALYSIS

This section evaluates our proposed C²U-MPPI in simulated corridors with varying pedestrian densities and through real-world demonstrations in a human-shared indoor environment.

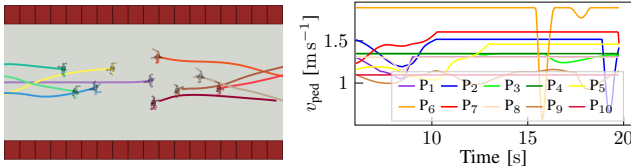
A. Simulation-Based Evaluation

1) *Simulation Setup:* In this study, extensive simulations are conducted using the fully autonomous ClearPath Jackal robot, which follows the differential wheeled robot kinematic model described in [21]. This kinematic model, with the system state $\mathbf{x} = [x, y, \theta]^T$ and control input $\mathbf{u} = [v, \omega]^T$, representing the robot's linear and angular velocities, is used to sample trajectories in MPPI and propagate sigma points in the proposed C²U-MPPI control strategy. Our Jackal robot is equipped with a 16-beam Velodyne LiDAR for obstacle detection in its surroundings. We employ Pedsim², an open-source ROS simulator based on the social forces model [22], to simulate realistic pedestrian interactions.

To demonstrate the effectiveness of sampling-based MPC strategies over gradient-based methods, we benchmark the proposed C²U-MPPI against log-MPPI [21] and MPCC [5]. For MPCC, we adopt its default configuration, which includes a predefined static obstacle map, a waypoint-based global path, and pedestrian positions generated by Pedsim, along with their predicted paths using an LKF. To ensure a fair comparison, both log-MPPI and C²U-MPPI simulations were conducted using the same hyperparameter settings specified in [12], including the UT, local costmap, and Savitzky-Golay (SG) filter parameters, with two exceptions: (i) a 7 s prediction horizon and 30 Hz control frequency were used, resulting in $N = 210$, and (ii) for log-MPPI, the hyperparameters λ , Σ_n , and $R = \lambda \Sigma_n^{-\frac{1}{2}}$ were tuned based on extensive simulations detailed in [21] to optimize performance. Both algorithms were executed in *real-time* on an NVIDIA GeForce GTX 1660 Ti laptop GPU using the PyCUDA module and integrated with the ROS framework. The cost functions' parameters are specified as follows: q_{goal} employs $Q = \text{Diag}(8, 8, 2)$; q_{stc} is assigned $w_{\text{stc}} = 10^3$; q_{exp} is configured with $w_{\text{exp}} = 500$,

¹In U-MPPI, \mathbf{x}_k and \mathbf{p}_k in q_{exp} and q_{rep} are replaced by $\mathcal{X}_k^{(i)}$ and $\mathbf{p}_k^{(i)}$.

²Pedestrian simulator code: https://github.com/srl-freiburg/pedsim_ros



(a) 10-pedestrian corridor environment (b) 10-pedestrian velocity profiles

Fig. 2: Snapshot of (a) our simulated corridor environment with 10 pedestrians moving at different speeds along the corridor, and (b) the velocity profiles of each pedestrian at 100% of their maximum speed.

$\alpha_{\text{exp}} = 40$, and $r_{\text{safe}}^i = 1$ m for lower-speed scenario (*Scenario #1*, as described in Section IV-A2), while $r_{\text{safe}}^i = 1.1$ m is used for high-speed scenarios (*Scenarios #2 and #3*); for q_{rep} , the parameters are $w_{\text{rep}} = 50$ and $\gamma_{\text{rep}} = 0.3$; and q_{prob} is assigned $w_{\text{prob}} = 10^3$, $\delta = 0.01$, $r_r = 0.2$ m, with $\Sigma_0^x = 0.001\mathbf{I}_3$ and $\Sigma_0^y = \mathbf{I}_2$, where \mathbf{I}_n denotes an $n \times n$ identity matrix.

2) *Simulation Scenarios and Performance Metrics*: For performance evaluation, we utilize a $30 \text{ m} \times 6 \text{ m}$ corridor environment featuring pedestrian groups of either 6 or 10 individuals (Fig. 2 provides an example of a 10-pedestrian setup). In each configuration, half of the pedestrians move along the corridor in one direction and the other half in the opposite direction, as illustrated in Fig. 2(a), with pedestrians moving at varying speeds to simulate realistic interactions, as depicted in Fig. 2(b). Pedestrians' trajectories are strategically set to ensure even distribution across the environment and intersections with the robot's target poses, enhancing scenario complexity. For instance, in the 10-pedestrian setup, at least four individuals cross or reach the robot's destinations, enabling dynamic interaction and collision avoidance while testing the robot's response to approaching pedestrians when stationary. To evaluate the performance of the proposed strategies, we consider three scenarios with varying reference speeds for both the robot and pedestrians, along with two distinct interaction modes. In the first scenario, denoted as *Scenario #1* (30%, 1), the robot's maximum speed is set to 1 m s^{-1} , with each pedestrian moving at 30% of their maximum speed. In *Scenario #2* (80%, 1.5), the robot's maximum speed is increased to 1.5 m s^{-1} , while pedestrians move at 80% of their maximum speed. Finally, in *Scenario #3* (100%, 2), the robot reaches a maximum speed of 2 m s^{-1} , and each pedestrian operates at full speed. Additionally, each scenario includes two interaction modes: *non-cooperative mode (NCM)*, where pedestrians move independently without regard for the robot, and *cooperative mode (CM)*, where pedestrians adjust their movements to avoid the robot's trajectory using social force dynamics. To ensure a fair performance comparison, two key aspects are considered across all conducted simulations: (i) the robot's objective is to sequentially reach specific target poses, beginning at $G_1 = [0 \text{ m}, -1 \text{ m}, 0^\circ]$, moving to $G_2 = [30 \text{ m}, 1 \text{ m}, 100^\circ]$, and finally returning to the origin, thereby promoting dynamic interactions with pedestrians to evaluate the robustness of the control strategies; and (ii) the dynamic collision cost is defined as $q_{\text{dyn}} = q_{\text{exp}} + q_{\text{rep}}$ in both log-MPPI and U-MPPI, with $\gamma = 1$ (denoted as U-MPPI¹) and $\gamma = -1$ (U-MPPI⁻¹), representing optimal cost settings for our specified scenarios and environment, while C²U-MPPI applies $q_{\text{dyn}} = q_{\text{prob}}$ with a 2-second pedestrian prediction horizon, denoted as $N_p = 2$ s. It is essential to highlight that while the dynamic obstacle

TABLE I: MPCC and log-MPPI performance statistics across ten trials in a cooperative mode (CM) with 10 pedestrians.

Scheme	\mathcal{N}_c	E_{dyn}	$10 \times J_{\text{acc}}$ [N]	v_{av} [m s^{-1}]	d_{av} [m]	t_{exec} [ms]
Scenario #1: (30%, 1), Cooperative Mode (CM)						
MPCC	0	0.73 ± 0.06	32.9 ± 4.8	0.73 ± 0.10	67.1 ± 1.5	5.3 ± 0.6
log-MPPI	0	0.34 ± 0.07	9.6 ± 2.7	0.77 ± 0.07	66.4 ± 3.7	9.8 ± 0.4
Scenario #2: (80%, 1.5), Cooperative Mode (CM)						
MPCC	0	0.74 ± 0.07	51.5 ± 4.2	1.22 ± 0.08	67.0 ± 2.2	4.3 ± 0.8
log-MPPI	0	0.26 ± 0.02	13.7 ± 2.3	1.23 ± 0.03	62.5 ± 0.7	8.9 ± 0.5
Scenario #3: (100%, 2), Cooperative Mode (CM)						
MPCC	0	0.74 ± 0.03	58.7 ± 8.0	1.46 ± 0.17	66.6 ± 2.8	4.8 ± 1.7
log-MPPI	0	0.32 ± 0.04	16.4 ± 1.4	1.56 ± 0.05	63.3 ± 1.4	9.1 ± 0.5

representation from Section III-D is compatible with log-MPPI and the two U-MPPI variants, our evaluation excluded any pedestrian prediction horizon, thus demonstrating robustness relative to MPCC, which applies $N_p = 3$ s.

To assess autonomous navigation in dynamic settings, we employ metrics for motion safety, robot trajectory quality, and control smoothness, focusing exclusively on the robot's trajectory and excluding pedestrian comfort, as we prioritize NCM over CM, as will be discussed in Section IV-A3. Motion safety, represented by the average number of collisions \mathcal{N}_c , indicates obstacle avoidance effectiveness, while robot trajectory quality, measured by the average distance traversed d_{av} , average robot speed v_{av} , and average dynamic energy E_{dyn} , captures path efficiency and energy consumption. Control smoothness, characterized by average accumulated jerk J_{acc} and average execution time per iteration t_{exec} , reflects the control system's stability and real-time adaptability. As most metrics are detailed in [12], only E_{dyn} and J_{acc} are defined here. $E_{\text{dyn}} = \frac{1}{N_t} \sum_{i=1}^{N_t} \left(\frac{v_{\text{peak}} - v_i}{v_{\text{peak}}} \right)^2$ quantifies energy consumption by averaging the deviation of instantaneous speed v_i from the peak speed $v_{\text{peak}} = \max_{i \leq N_t} v_i$, while $J_{\text{acc}} = \frac{1}{N_t} \sum_{i=1}^{N_t} j_i$, where N_t denotes the number of discrete time steps in the trajectory, and j_i represents the instantaneous jerk. Lower values of E_{dyn} and J_{acc} indicate improved performance, reflecting efficient energy use and smooth control.

3) *Simulation Results*: Tables I, II, and III present 10-trial averaged performance statistics for the proposed control strategies in goal-oriented navigation, evaluated across our pre-defined scenarios within 6- and 10-pedestrian environments. Table I serves as an example comparison of gradient-based (MPCC) and sampling-based (log-MPPI) methods in CM within a 10-pedestrian environment, excluding C²U-MPPI, as log-MPPI represents a worst-case scenario for sampling-based methods with no pedestrian prediction ($N_p = 0$ s). Notably, both control strategies achieve collision-free navigation across all scenarios; however, log-MPPI demonstrates enhanced efficiency and smoothness, reflected in its lower averages in accumulated jerk J_{acc} , distance traveled d_{av} , and dynamic energy E_{dyn} , alongside a higher average speed v_{av} . Although CM reflects realistic conditions where pedestrians adaptively avoid the robot, it does not provide a rigorous assessment of control robustness. Therefore, our primary analysis focuses on NCM, where pedestrians move independently, challenging the control strategy's collision avoidance capabilities and adaptability under uncooperative conditions. Building on these insights, Table II presents results in NCM with 6 pedestrians, comparing

TABLE II: Performance statistics of the three proposed control strategies in a non-cooperative 6-pedestrian mode (NCM).

Scheme	\mathcal{N}_c	E_{dyn}	$10 \times J_{\text{acc}}$ [N]	v_{av} [m s ⁻¹]	d_{av} [m]	t_{exec} [ms]
Scenario #1: (30%, 1), Non-Cooperative Mode (NCM)						
MPCC	1	0.64 ± 0.17	38.0 ± 9.9	0.87 ± 0.06	67.3 ± 1.6	4.8 ± 0.8
log-MPPI	0	0.24 ± 0.03	12.0 ± 3.9	0.86 ± 0.01	63.0 ± 0.9	8.0 ± 0.4
Ours	0	0.27 ± 0.04	10.2 ± 1.4	0.86 ± 0.01	62.9 ± 1.1	9.0 ± 0.2
Scenario #2: (80%, 1.5), Non-Cooperative Mode (NCM)						
MPCC	7	0.70 ± 0.20	50.2 ± 9.7	1.22 ± 0.09	68.7 ± 2.8	3.0 ± 0.9
log-MPPI	1	0.27 ± 0.02	15.2 ± 4.6	1.23 ± 0.02	63.5 ± 1.1	8.2 ± 0.5
Ours	0	0.28 ± 0.05	14.4 ± 2.2	1.25 ± 0.02	63.4 ± 1.6	9.1 ± 0.5
Scenario #3: (100%, 2), Non-Cooperative Mode (NCM)						
MPCC	4	0.71 ± 0.16	60.8 ± 12.9	1.47 ± 0.09	69.1 ± 2.4	3.2 ± 0.4
log-MPPI	1	0.32 ± 0.03	18.3 ± 6.5	1.54 ± 0.05	63.7 ± 1.3	8.2 ± 0.3
Ours	0	0.29 ± 0.04	17.3 ± 2.6	1.62 ± 0.07	62.8 ± 1.4	8.9 ± 0.4

the three control strategies. In this uncooperative setting, our proposed C²U-MPPI framework notably outperforms MPCC and log-MPPI in collision avoidance, achieving zero collisions across all scenarios. It also demonstrates lower J_{acc} and d_{av} , particularly compared to MPCC, while maintaining a higher speed profile in *Scenarios #2* and *#3*, reflecting smoother control actions and more efficient path planning at higher speeds. While log-MPPI achieves slightly lower E_{dyn} in the first two scenarios, the proposed method effectively balances collision avoidance with safe and efficient robot trajectory in complex, uncooperative environments, thanks to its integration of the pedestrian prediction horizon and uncertainty propagation within the dynamic cost q_{dyn} .

In Table III, the analysis extends to the established 10-pedestrian environment, incorporating the two U-MPPI variants: U-MPPI⁻¹ and U-MPPI¹. Notably, both U-MPPI variants outperform MPCC and log-MPPI in achieving fewer collisions \mathcal{N}_c across all scenarios, while demonstrating shorter routes to the goal, particularly in *Scenarios #2* and *#3*, due to their efficient sampling strategy and integration of risk-sensitive trajectory evaluation, as described in (7). Our method consistently achieves the lowest collision rates across all scenarios, with high trajectory quality in *Scenario #1*, as reflected by shorter d_{av} . However, in *Scenarios #2* and *#3*, trajectory efficiency declines, with d_{av} exceeding that of all other methods in *Scenario #2* and the U-MPPI variants in *Scenario #3*. This reduction in efficiency results from setting r_r to 0.3 m, rather than the default 0.2 m, to enhance safety in high-speed scenarios. Our empirical observations in this crowded corridor environment revealed that increasing both r_r and N_p leads the robot to yield more space to pedestrians. For example, we observed instances where the robot occasionally moved backward to avoid collisions, particularly when approaching one of its goals such as G_2 or when encountering oncoming pedestrian groups. This behavior, as shown in the supplementary video, increased the traveled distance d_{av} while prioritizing pedestrian safety.

Reducing N_p has shown promise in improving performance, as demonstrated in Test #1 of Table IV. By setting $N_p = 1$ instead of the default $N_p = 2$ for *Scenario #3*, we observed a high-quality trajectory with $d_{\text{av}} = 66.7$ m, compared to 68.6 m with $N_p = 2$, along with smoother control actions. Tests #2 and #3 further explored performance adjustments by setting $N_p = 0$ (no prediction) and varying γ values

TABLE III: Performance statistics of the three control strategies, including U-MPPI with $\gamma = -1$ (U-MPPI⁻¹) and $\gamma = 1$ (U-MPPI¹), in a non-cooperative 10-pedestrian mode (NCM).

Scheme	\mathcal{N}_c	E_{dyn}	$10 \times J_{\text{acc}}$ [N]	v_{av} [m s ⁻¹]	d_{av} [m]	t_{exec} [ms]
Scenario #1: (30%, 1), Non-Cooperative Mode (NCM)						
MPCC	3	0.74 ± 0.12	36.8 ± 7.3	0.74 ± 0.12	72.2 ± 5.9	6.4 ± 1.2
log-MPPI	1	0.35 ± 0.04	9.6 ± 1.9	0.71 ± 0.04	76.6 ± 3.1	9.8 ± 0.4
U-MPPI ⁻¹	1	0.36 ± 0.04	10.0 ± 3.4	0.71 ± 0.03	76.8 ± 3.3	13.1 ± 0.5
U-MPPI ¹	1	0.36 ± 0.05	8.9 ± 2.3	0.70 ± 0.05	75.0 ± 3.9	12.7 ± 0.3
Ours	0	0.35 ± 0.02	9.2 ± 1.1	0.72 ± 0.04	68.9 ± 1.2	11.0 ± 0.5
Scenario #2: (80%, 1.5), Non-Cooperative Mode (NCM)						
MPCC	9	0.71 ± 0.13	45.4 ± 9.1	1.10 ± 0.10	70.5 ± 1.3	6.0 ± 1.1
log-MPPI	4	0.29 ± 0.04	16.0 ± 4.3	1.19 ± 0.06	68.6 ± 3.9	9.9 ± 0.6
U-MPPI ⁻¹	2	0.26 ± 0.04	12.8 ± 1.5	1.22 ± 0.04	67.1 ± 3.7	12.5 ± 0.6
U-MPPI ¹	3	0.29 ± 0.03	12.6 ± 0.8	1.17 ± 0.04	67.7 ± 2.8	12.7 ± 0.3
Ours	1	0.31 ± 0.04	17.8 ± 4.6	1.16 ± 0.07	72.4 ± 9.3	10.9 ± 0.4
Scenario #3: (100%, 2), Non-Cooperative Mode (NCM)						
MPCC	17	0.75 ± 0.11	53.3 ± 13.4	1.35 ± 0.14	71.7 ± 3.4	6.2 ± 1.2
log-MPPI	5	0.34 ± 0.03	16.6 ± 4.3	1.44 ± 0.07	69.9 ± 5.6	10.1 ± 0.5
U-MPPI ⁻¹	3	0.34 ± 0.07	16.3 ± 1.6	1.46 ± 0.10	66.9 ± 2.2	12.7 ± 0.4
U-MPPI ¹	4	0.34 ± 0.04	15.6 ± 4.3	1.42 ± 0.09	67.4 ± 3.5	12.8 ± 0.5
Ours	0	0.33 ± 0.02	17.5 ± 1.8	1.44 ± 0.09	68.6 ± 4.6	11.4 ± 0.4

($\gamma = 1$ in Test #2 and $\gamma = -1$ in Test #3). We note that reducing N_p to 0 led to a decline in performance, indicating that some level of pedestrian prediction is essential to maintain trajectory efficiency and control quality. Moreover, it is evident from Table III that the U-MPPI variants perform similarly, due to assigning a higher value to Q . To further examine this effect, Tests #4, #5, and #6 replicate the simulations from *Scenario #3* with a reduced $Q = \text{Diag}(2.5, 2.5, 2)$ for log-MPPI, U-MPPI⁻¹, and U-MPPI¹, respectively. This reduction in Q results in slower robot convergence to the goals, causing oscillatory motion around the desired pose as the robot continually adjusts to avoid nearby agents, ultimately leading to a significantly longer trajectory. In Test #5, however, we observe a higher-quality trajectory compared to the other two tests, as in this setting Q_{rs} increases with rising uncertainty levels, imposing greater penalties for deviations from the desired state, thereby reducing oscillations and yielding a more efficient trajectory. Throughout all conducted simulations, MPCC exhibits higher E_{dyn} and J_{acc} due to its effort to balance path-following with collision avoidance, leading to sharp trajectory adjustments, increased energy consumption, and motion discontinuities in dynamic environments. Additionally, all sampling-based approaches consistently achieve real-time performance, with $t_{\text{exec}} < 33.3$ ms, regardless of whether the optimization problem involves 6 or 10 pedestrians. In contrast, MPCC demonstrates real-time performance only when limited to 6 pedestrians (see [5] for details). Notably,

TABLE IV: Impact of lower N_p and reduced Q on sampling-based control strategies in a 10-pedestrian NCM setup.

Test #	\mathcal{N}_c	E_{dyn}	$10 \times J_{\text{acc}}$ [N]	v_{av} [m s ⁻¹]	d_{av} [m]	t_{exec} [ms]
Scenario #3: (100%, 2), Lower N_p						
Test #1	0	0.31 ± 0.03	16.3 ± 1.5	1.48 ± 0.06	66.7 ± 2.6	10.8 ± 0.4
Test #2	2	0.33 ± 0.03	17.2 ± 5.8	1.46 ± 0.07	69.6 ± 6.3	11.2 ± 0.8
Test #3	3	0.32 ± 0.02	15.1 ± 1.3	1.49 ± 0.08	69.9 ± 5.6	10.5 ± 0.6
Scenario #3: (100%, 2), $Q = (2.5, 2.5, 2)$						
Test #4	3	0.44 ± 0.11	15.7 ± 5.7	1.20 ± 0.24	74.8 ± 5.7	12.8 ± 0.4
Test #5	2	0.37 ± 0.09	16.5 ± 7.3	1.34 ± 0.20	70.1 ± 6.8	12.8 ± 0.5
Test #6	3	0.43 ± 0.14	16.6 ± 7.1	1.23 ± 0.29	73.5 ± 11.6	12.2 ± 0.7

TABLE V: Performance statistics of C²U-MPPI with 5 pedestrians.

N_p [s]	\mathcal{N}_c	E_{dyn}	$10 \times J_{\text{acc}}$ [N]	v_{av} [m s ⁻¹]	d_{av} [m]	t_{exec} [ms]
1	1	0.45 ± 0.11	21.4 ± 1.6	0.75 ± 0.04	20.2 ± 2.3	13.17 ± 0.12
0	2	0.55 ± 0.21	29.7 ± 4.3	0.74 ± 0.06	27.4 ± 3.2	13.01 ± 0.30

our method, utilizing $N_p = 2$ s, achieves execution times comparable to log-MPPI, which operates with $N_p = 0$ s, owing to the dynamic obstacle representation and optimized thread utilization inherent in the U-MPPI framework (refer to [12] for details). However, the U-MPPI variants exhibit higher t_{exec} values, even with $N_p = 0$ s, due to their reliance on q_{exp} , which imposes a greater computational burden per thread compared to the lightweight indicator function q_{prob} used in our method.

To sum up, it is not surprising that sampling-based methods outperform gradient-based approach, as they leverage a broader exploration of the control space and are inherently more robust to the nonlinearities and uncertainties present in dynamic environments. Furthermore, their ability to generate feasible solutions while maintaining minimal constraint violations enhances their adaptability and efficiency in real-time navigation scenarios. This advantage is particularly evident in examples such as *Scenario #3* with the 10-pedestrian setup, where MPCC produces infeasible solutions that violate the linear velocity constraint by more than 20% across the 10 trials, compared to less than 1% in C²U-MPPI.

B. Real-World Demonstration

1) *Experimental Setup and Validation Environment*: The simulation setup from Section IV-A1 is adapted for experimental validation with two modifications: (i) the robot’s maximum speed is set to 1 m s⁻¹, while human agents have average maximum speeds ranging from 0.6 m s⁻¹ to 1.3 m s⁻¹; (ii) agents’ localization and tracking are obtained using a 12-camera Vicon motion capture system. The performance evaluation is carried out in a 7 m × 5.5 m rectangular workspace, populated with five pedestrians navigating between opposing corners, thereby creating collision-avoidance challenges. The robot is tasked with navigating from the initial position $\mathbf{x}_s = [0 \text{ m}, 0 \text{ m}, 0^\circ]^\top$ to the target $\mathbf{x}_f = [6.5 \text{ m}, 4.5 \text{ m}, 50^\circ]^\top$ and returning to \mathbf{x}_s .

2) *Experimental Results*: The performance statistics of C²U-MPPI, based on six trials conducted in the indoor environment, are summarized in Table V for $N_p = 1$ s and $N = 0$ s. Based on the trials, we can conclude that incorporating pedestrian predictions $N_p = 1$ s enhances dynamic energy efficiency E_{dyn} and control smoothness J_{acc} compared to $N_p = 0$ s, with a marginal increase in average velocity v_{av} and fewer collisions \mathcal{N}_c . However, the robot’s average distance traversed d_{av} is lower, reflecting a trade-off between trajectory efficiency and safety. Execution times t_{exec} remain consistent, supporting real-time operation of the control algorithm.

V. CONCLUSION

In this letter, we established that robust probabilistic collision avoidance in human-shared environments can be effectively achieved via a chance-constrained U-MPPI framework, where probabilistic collision checking is reformulated as deterministic constraints for seamless integration. Our control framework robustly integrates predictive motion uncertainties, risk-aware constraints, and a layered dynamic obstacle representation, enabling efficient multi-obstacle handling while enhancing safety and computational efficiency. Extensive simulations and

experimental results demonstrate its superiority over baseline methods in terms of collision avoidance, trajectory efficiency, and real-time adaptability within dense crowds. Future work will focus on extending the framework to multi-agent systems.

REFERENCES

- [1] P. T. Singamaneni, P. Bachiller-Burgos, L. J. Manso, A. Garrell, A. Sanfeliu, A. Spalanzani, and R. Alami, “A survey on socially aware robot navigation: Taxonomy and future challenges,” *Int. J. Robot. Res.*, 2024.
- [2] G. Ferrer, A. Garrell, and A. Sanfeliu, “Robot companion: A social-force based approach with human awareness-navigation in crowded environments,” in *Proc. IEEE/RSJ Int. Conf. Intell. Robots Syst.*, 2013, pp. 1688–1694.
- [3] O. Khatib, “Real-time obstacle avoidance for manipulators and mobile robots,” *Int. J. Robot. Res.*, vol. 5, no. 1, pp. 90–98, 1986.
- [4] Y. F. Chen, M. Everett, M. Liu, and J. P. How, “Socially aware motion planning with deep reinforcement learning,” in *Proc. IEEE/RSJ Int. Conf. Intell. Robots Syst.*, 2017, pp. 1343–1350.
- [5] B. Brito, B. Floor, L. Ferranti, and J. Alonso-Mora, “Model predictive contouring control for collision avoidance in unstructured dynamic environments,” *IEEE Robot. Autom. Lett.*, pp. 4459–4466, 2019.
- [6] Y. Chen, F. Zhao, and Y. Lou, “Interactive model predictive control for robot navigation in dense crowds,” *IEEE Transactions on Systems, Man, and Cybernetics: Systems*, vol. 52, no. 4, pp. 2289–2301, 2021.
- [7] E. Stefanini, L. Palmieri, A. Rudenko, T. Hielscher, T. Linder, and L. Pallottino, “Efficient context-aware model predictive control for human-aware navigation,” *IEEE Robot. Autom. Lett.*, 2024.
- [8] Z. Jian, Z. Yan, X. Lei, Z. Lu, B. Lan, X. Wang, and B. Liang, “Dynamic control barrier function-based model predictive control to safety-critical obstacle-avoidance of mobile robot,” in *Proc. IEEE Int. Conf. Robot. Automat.*, 2023, pp. 3679–3685.
- [9] Z. Lu, K. Feng, J. Xu, H. Chen, and Y. Lou, “Robot safe planning in dynamic environments based on model predictive control using control barrier function,” *arXiv preprint arXiv:2404.05952*, 2024.
- [10] N. E. Du Toit and J. W. Burdick, “Probabilistic collision checking with chance constraints,” *IEEE Trans. Robot.*, pp. 809–815, 2011.
- [11] H. Zhu and J. Alonso-Mora, “Chance-constrained collision avoidance for MAVs in dynamic environments,” *IEEE Robot. Autom. Lett.*, vol. 4, no. 2, pp. 776–783, 2019.
- [12] I. S. Mohamed, J. Xu, G. Sukhatme, and L. Liu, “Towards efficient MPPI trajectory generation with unscented guidance: U-MPPI control strategy,” *IEEE Trans. Robot. (T-RO)*, 2024, Accepted.
- [13] J. Zeng, Z. Li, and K. Sreenath, “Enhancing feasibility and safety of nonlinear model predictive control with discrete-time control barrier functions,” in *Proc. IEEE Conf. Decis. Control*, 2021, pp. 6137–6144.
- [14] H. Ma, X. Zhang, S. E. Li, Z. Lin, Y. Lyu, and S. Zheng, “Feasibility enhancement of constrained receding horizon control using generalized control barrier function,” in *Proc. IEEE Int. Conf. Ind. Cyber-Phys. Syst.*, 2021, pp. 551–557.
- [15] K. A. Mustafa, O. de Groot, X. Wang, J. Kober, and J. Alonso-Mora, “Probabilistic risk assessment for chance-constrained collision avoidance in uncertain dynamic environments,” in *Proc. IEEE Int. Conf. Robot. Automat.*, 2023, pp. 3628–3634.
- [16] M. Castillo-Lopez, P. Ludvig, S. A. Sajadi-Alamdari, J. L. Sanchez-Lopez, M. A. Olivares-Mendez, and H. Voos, “A real-time approach for chance-constrained motion planning with dynamic obstacles,” *IEEE Robot. Autom. Lett.*, vol. 5, no. 2, pp. 3620–3625, 2020.
- [17] K. Ryu and N. Mehr, “Integrating predictive motion uncertainties with distributionally robust risk-aware control for safe robot navigation in crowds,” *arXiv preprint arXiv:2403.05081*, 2024.
- [18] I. S. Mohamed, G. Allibert, and P. Martinet, “Model predictive path integral control framework for partially observable navigation: A quadrotor case study,” in *Proc. IEEE 16th Int. Conf. Control, Automat., Robot. Vis.*, 2020, pp. 196–203.
- [19] R. E. Kalman, “A new approach to linear filtering and prediction problems,” *Trans. ASME J. Basic Eng.*, vol. 82, no. 1, pp. 35–45, 1960.
- [20] G. Williams, A. Aldrich, and E. A. Theodorou, “Model predictive path integral control: From theory to parallel computation,” *Journal of Guidance, Control, and Dynamics*, vol. 40, no. 2, pp. 344–357, 2017.
- [21] I. S. Mohamed, K. Yin, and L. Liu, “Autonomous navigation of AGVs in unknown cluttered environments: log-MPPI control strategy,” *IEEE Robot. Autom. Lett.*, vol. 7, no. 4, pp. 10 240–10 247, 2022.
- [22] D. Helbing and P. Molnar, “Social force model for pedestrian dynamics,” *Physical review E*, vol. 51, no. 5, p. 4282, 1995.